Exp Fluids (2013) 54:1447
DOI 10.1007/s00348-012-1447-5

RESEARCH ARTICLE

On the competition between leading-edge and tip-vortex growth for a pitching plate

Colin Hartloper · Matthias Kinzel · David E. Rival

Received: 25 August 2012 / Revised: 15 November 2012 / Accepted: 12 December 2012 / Published online: 27 December 2012

Abstract The interaction between leading-edge-vortex and tip-vortex development on a low-aspect-ratio plate has been investigated and compared to a nominally two-dimensional rectangular flat plate. Simultaneous to force measurements, three-dimensional particle tracking velocimetry (3D-PTV) was used to characterize the instantaneous flow field on the suction side. An integration of the spanwise circulation distribution for the two-dimensional case indicates that the leading-edge-vortex formation process is correlated with the convective time and not with the instantaneous pitch angle. However, for the finite plate, it is found that the tip-vortex formation process is correlated with the instantaneous pitch angle instead. Since leading-edge vorticity is convected inboard by tip-vortex-induced spanwise velocity, leading-edge-vortex growth is found to be retarded in the tip region. Finally, with the aid of Lagrangian particle tracks, the leading-edge and tip vortices are found to grow distinct from one another, that is, no leading-edge vorticity is drawn into the tip vortex. However, the tip vortex is found to influence the leading-edge-vortex dynamics through inboard transport of leading-edge vorticity and is therefore responsible for vortex compression at the mid-span.

C. Hartloper · D. E. Rival (✉)
Department of Mechanical Engineering, University of Calgary, Calgary, AB, Canada
e-mail: derival@ucalgary.ca

M. Kinzel
Graduate Aerospace Laboratories of the California Institute of Technology, Pasadena, CA, USA

1 Introduction

The interaction between leading-edge vortex (LEV) and tip-vortex (TV) development plays a primary role in the unsteady loadings of flapping flight and propulsion for micro aerial vehicles and underwater autonomous vehicles, respectively, as well as for wind turbines and propellers exposed to dynamic-inflow conditions. Coherent structures such as leading-edge and tip vortices form during rapid changes in the pressure difference between the suction and pressure sides of wings and blades and are fed from shear layers formed at their respective edges. Despite the critical influence of these vortical structures on instantaneous forces, our ability to control their growth and separation remains elusive. A recent study by Baik et al. (2012) combined pitching and plunging to maintain a constant angle of attack history and found that, on a two-dimensional flat plate undergoing deep-stall oscillations, the effective angle of attack and reduced frequency determine the instantaneous flow evolution. However, for the finite-wing case, Birch and Lee (2005) studied the near-wake tip vortex of a NACA0015 wing undergoing both light and deep-stall oscillations and found that the growth of the tip vortex was insensitive to changes in pitch angle.

Furthermore, studies by Ringuette et al. (2007) and Kim and Gharib (2011) investigated the leading-edge-vortex and tip-vortex development on low-aspect-ratio flat plates towed from rest at a 90° angle of attack. It was found that the tip vortex increased the overall drag and that this force increased with lower aspect ratios. In addition, it was observed that the circulation of the leading-edge vortex decreased at spanwise positions close to the tip. This observation is in agreement with recent results from Jardin et al. (2012), which identified that the leading-edge-vortex development on a NACA0012 undergoing translation at a

high angle of attack can be divided into three regions: the two-dimensional, transition and near-tip regions. This near-tip region was characterized by the inhibition of leading-edge-vortex growth via tip effects. Kim and Gharib (2010) also compared the leading-edge-vortex and tip-vortex development on flat plates undergoing rotation and translation at high angles of attack and found that the vortical structures were more pronounced near the tip for plates undergoing rotation.

When performing a pitch and return experiment on an aspect-ratio-two (AR=2) rectangular flat plate, Yilmaz et al. (2010) observed that variations in the pitch rate and pitch location resulted in a time shift in the flow-field evolution, but had little effect on the late-stage form of the leading-edge vortex. In a separate study, Yilmaz and Rockwell (2012) presented phase-averaged, three-dimensional flow structures showing the leading-edge-vortex and tip-vortex growth on rectangular and elliptical flat plates of aspect ratio two undergoing a pitching motion. In this study, a leading-edge-vortex eruption was observed, which was found to be less pronounced for the elliptical planform. The experimental results of Yilmaz and Rockwell (2012) are further supported by high-fidelity numerical simulations performed by Visbal (2011) on a plunging flat plate of aspect ratio two, which identify an arched shape to the leading-edge vortex prior to the leading-edge-vortex eruption. The growth of such an arched-shape leading-edge vortex has been further studied by Barnes and Visbal (2012), and a more recent numerical investigation performed by Visbal (2012) on an aspect-ratio-two rectangular flat plate undergoing a pitch up motion found that an increase in pitch rate resulted in a phase delay in the flow-field evolution. The leading-edge-vortex eruption observed on pitching and plunging flat plates is in contrast to the somewhat stable, attached leading-edge vortex which was qualitatively observed by Lentink and Dickinson (2009) on a revolving model fly wing and more recently quantified by Ozen and Rockwell (2012), Carr et al. (2012) and Garmann et al. (2012) on a revolving flat plate.

From these above-mentioned studies, it is evident that a strong time-dependent, three-dimensional interaction between the vortical structures exists. Thus, similar to the analysis performed by Beem et al. (2012) when investigating the growth of such structures, three-dimensional vorticity transport must be considered. The vorticity transport equation in tensor notation is given as:

$$\frac{\partial \omega_i}{\partial t} + u_j \frac{\partial \omega_i}{\partial x_j} = \omega_j \frac{\partial u_i}{\partial x_j} + \nu \frac{\partial^2 \omega_i}{\partial x_j \partial x_j}, \tag{1}$$

where the terms from left to right are the local unsteady change in vorticity, vortex convection, vortex stretching and tilting, and the viscous diffusion of vorticity. In the leading-edge and tip-vortex formation, it is assumed that the timescales of diffusion are much slower than for the vortex growth and convection, and thus the diffusion term can be neglected. From the solution of the classical lifting-line formulation, only the component of vorticity oriented parallel to the spanwise axis (z-axis) contributes to lift generation. The z-vorticity transport equation can be expanded as:

$$\frac{\partial \omega_z}{\partial t} + u \frac{\partial \omega_z}{\partial x} + v \frac{\partial \omega_z}{\partial y} + w \frac{\partial \omega_z}{\partial z} = \omega_x \frac{\partial w}{\partial x} + \omega_y \frac{\partial w}{\partial y} + \omega_z \frac{\partial w}{\partial z}, \tag{2}$$

where the right-hand terms represent x-tilting, y-tilting and z-stretching, respectively. Pitt-Ford and Babinsky (2012) recently performed an investigation comparing the growth of the leading-edge vortex, the bound vortex and the trailing-edge vortex of a nominally two-dimensional plate accelerated from rest at a 45° geometric angle of attack. Their results suggested that steady-state (stalled) lift was strongly correlated to the formation and shedding of a LEV and that the bound circulation was effectively negligible early on when the steady Kutta condition is violated. However, for the three-dimensional case of a low-aspect-ratio plate, it is suspected that vorticity transport between the leading-edge and tip vortices will have an impact on their respective development and thus the overall aerodynamic loads. For example, the z-convection term in Eq. 2 provides a means of redistributing z-vorticity and thus altering the spanwise circulation distribution. The x- and y-tilting terms in Eq. 2 are critical as they provide a means of converting z-vorticity from the leading edge into x- and y-vorticity in the tip vortex. Therefore, in a flow field with strong, three-dimensional vortex topology, as found on the suction side of a low-aspect-ratio plate, these tilting terms could potentially play an important role in the realignment and growth rates of both leading-edge and tip vortices. The z-stretching term in Eq. 2 is significant as it represents leading-edge-vortex stretching or compression when positive or negative, respectively. Leading-edge-vortex compression is of particular interest because it implies a concentration of the leading-edge vortex at the mid-span. A compressed leading-edge vortex would exhibit an arched shape similar to that observed by Yilmaz and Rockwell (2012) and Visbal (2011) on flat plates of aspect ratio two.

Some of the immediate questions that we attempt to address in this study are as follows: what are the time scales associated with the leading-edge-vortex and tip-vortex growth during a rapid change in incidence? In such unsteady cases do the leading-edge and tip vortices vary proportionally in strength to one another as expected from traditional lifting-line theory? Ultimately will it be possible to manipulate the vortex dynamics so as to control these rapid changes

in the boundary conditions? In the current study, we tackle these issues by comparing the vortex development for both nominally two-dimensional and low-aspect-ratio plates. In the process, we try to characterize the influence of the tip vortex on leading-edge-vortex growth for two distinct levels of unsteadiness. Furthermore, we try to quantify the degree of interaction between leading-edge and tip vortices at various stages in their development via vorticity transport arguments. In the following section, a detailed description of the experimental apparatus used to tackle this highly unsteady, three-dimensional problem is presented.

2 Methods

Experiments were performed in a free-surface water tunnel at the University of Calgary as shown in Fig. 1. The water tunnel has a rectangular cross section with a mean width of 385 mm and water depth of 432 mm. Two different plates were tested, one with a low-aspect ratio of four and the other with AR $= \infty$, that is, nominally two-dimensional. The plates were constructed from aluminium and had a thickness of 3.175 mm, which is approximately 6 % of chord. The aspect-ratio four plate was chosen as it represents a common planform for natural flyers where mid-span vortex interaction is expected to be weaker when compared to lower aspect ratios as in Yilmaz and Rockwell (2012). Both plates had a chord length $c = 50$ mm and square leading edges and trailing edges. The low-aspect-ratio plate had a span of $s = 200$ mm while the nominally two-dimensional plate had a physical span of $s = 435$ mm, which stretched from the bottom of the water tunnel (3-mm gap) to the free surface, see Fig. 2 for details regarding the plate positions with respect to the test section floor and free surface. The free-stream velocity of the water tunnel was set to $U_\infty = 0.2$m/s, thus providing a Reynolds number of $Re = 10{,}000$ based on the chord length. Both plates were pitched about the leading edge of the plate at two different pitch rates, pitching from a geometric angle of attack $\alpha = 0°$ to 45°. The pitch angle was increased according to a half-cosine curve, with the slow- and fast-pitching motions completing their kinematics in dimensionless times $t^* = tU_\infty/c = 6$ and $t^* = 1$, respectively. The equivalent reduced frequencies of the slow- and fast-pitching motions were $k = 0.26$ and $k = 1.57$, respectively, where $k = \pi fc/U_\infty$ and f is the frequency corresponding to a full cycle of the pitching motion.

Figure 2 shows an image (left) and schematic (right) of the experimental apparatus. An ATI Gamma six-component force and moment sensor placed at the base of the sting that holds the plate was used to measure the instantaneous forces throughout the pitching cycle. The force sensor was calibrated using the SI-32-2.5 calibration which provides a sensing range of 32 N at a resolution of 1/80 N. The raw lift and drag signals from the ATI sensor were filtered using a 25-Hz low-pass filter followed by a running-average filter in a procedure similar to that employed by Jones and Babinsky (2011). The inertia of the sting assembly was subtracted from the measured forces for each test case. The inertia of the plates was negligible in comparison with a mass approximately three times smaller than the sting assembly. Signals from multiple runs of the same test case are compared in Fig. 4 (a). Here, the repeatability of the measurements is demonstrated by comparing the lift coefficient of three runs of the same test case in which the average value of the normalized difference in lift coefficient is 5.9 %.

The three-dimensional particle tracking velocimetry (3D-PTV) technique, as described by Luethi et al. (2005), was used to quantify the flow field on the suction side of the pitching plates. This particle tracking technique provides a time-resolved Lagrangian view of the flow-field evolution. The direct access to the Lagrangian flow field

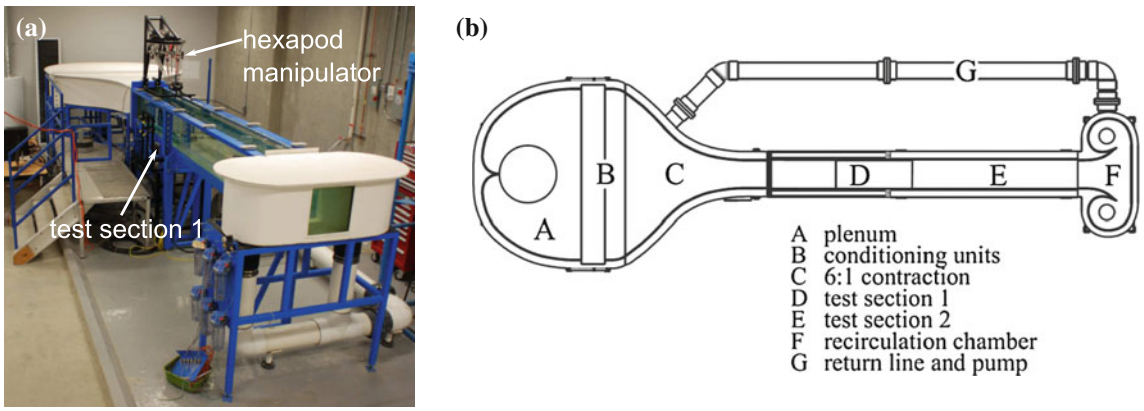

Fig. 1 **a** Image and **b** planview of the water tunnel used for 3D-PTV experiments. The pump, located at the base of the plenum, drives water through the contraction into the test sections and recirculation chamber. The test apparatus, which includes the hexapod manipulator shown in Fig. 2, was located in the middle of test Sect. 1

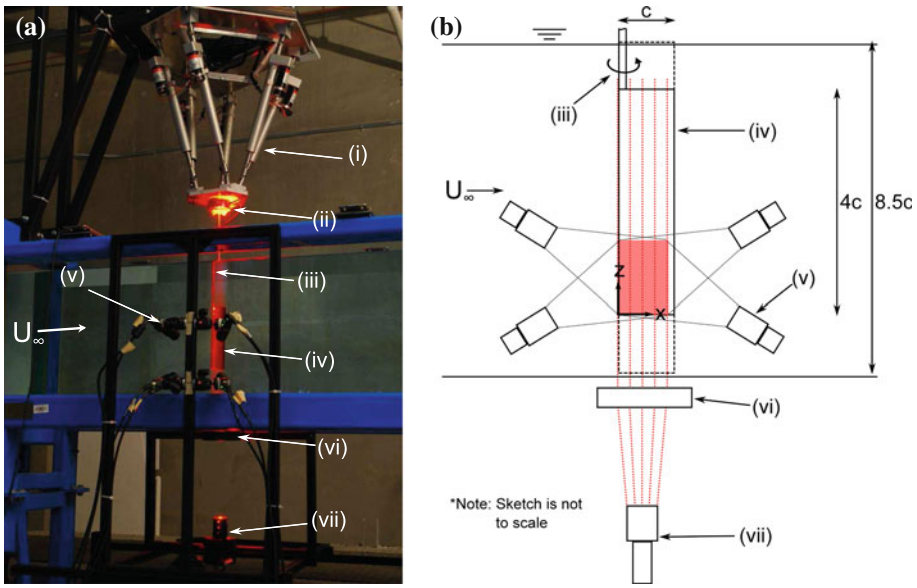

Fig. 2 **a** Image and **b** sketch of the experimental apparatus. The various system components are as follows: (i) 6 degree-of-freedom hexapod manipulator, (ii) 6-component ATI Gamma balance, (iii) sting, (iv) AR=4 plate, (v) 3D-PTV camera system, (vi) 300-mm focal length converging lens and (vii) overdriven LED. The measurement volume is indicated by the region shaded in red. The position of the nominally two-dimensional plate is shown in (**b**) by the *dashed black line*. The coordinate system used is shown on the *right* with the origin at the tip of the leading edge of the plate. The *y*-direction is positive into the page. Water flows in the positive *x*-direction at $U_\infty = 0.2$m/s and the plate rotates counterclockwise about the *z*-axis

allows the tracking of the fluid elements that produce the leading-edge and tip vortices. In addition, the accuracy of 3D-PTV is not effected by reflections from surfaces that are present in the measurement volume, see Kähler et al. (2012). In order to perform clear particle tracks, the water tunnel was seeded with 100μm silver-coated, hollow glass spheres. The seeding particles have a Stokes number of approximately 2.4×10^{-3} and therefore will follow the fluid accelerations accurately. The 3D-PTV measurement volume was limited to a rectangular prism of dimensions 40 mm × 40 mm × 80 mm, as shown in Fig. 3. For illumination, an overdriven LED was used to deliver a 2 W pulse over 1 ms at a wavelength of 630 nm. Based on a 1 ms exposure time, the particle streaking was estimated to be less than one pixel, which was confirmed upon inspection of the raw images. The plates were painted black to prevent light scattering, and together with precise alignment of the light source, no digital masking was necessary at the image-processing stage.

During the experiments, data were recorded with four Allied Vision Guppy PRO cameras. The cameras have a resolution of 640×480 pixel^2 and were operated at a frame rate of 120 Hz. The positions of the seeding particles were determined with a resolution finer than 0.2 mm and trajectories were constructed based on the methods described by Luethi et al. (2005). The Lagrangian velocities and accelerations were derived by differentiation of the particle tracks. The inter-particle distance, which

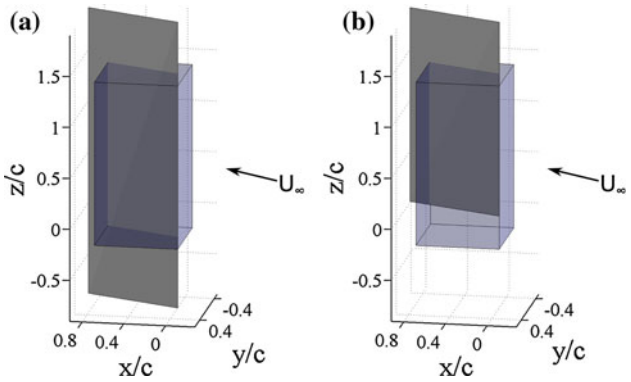

Fig. 3 The measurement volume for the **a** nominally two-dimensional and **b** low-aspect-ratio plates. For the low-aspect-ratio plate, the measurement volume extends from 1.4c inboard of the tip to 0.2c outboard of the tip. The origin is coincident with the leading edge and the tip edge. Plates shown at $\alpha = 22.5°$. Oncoming flow is in the positive *x*-direction as indicated by U_∞

determines the accuracy of the spatial derivatives, was approximately 5 mm during the experiments. The relative uncertainty in the particle track velocity was estimated to be $\delta u/u = \pm 0.01$ using the method described by Feng et al. (2011). The data were interpolated on to an Eulerian grid with a grid spacing of 5 mm. The velocity and velocity derivatives were obtained from weighted interpolations of the Lagrangian data in a sphere around each point. For further details, see Luethi et al. (2005) and Kinzel et al. (2011). The maximum measurable velocity, acceleration

and vorticity can be estimated from the camera frame rate, chip size, observation volume size and the average interparticle distance. The corresponding values are ±0.48 m/s, ±27 m/s^2 and ±50 s^{-1}, respectively. An estimate of the uncertainty in the velocity derivatives was made by comparing the Lagrangian acceleration $a_t = Du_i/Dt$ with the sum of the local acceleration $a_l = \partial u_i/\partial t$ and convective acceleration $a_c = u_j \partial u_i/\partial x_j$. The difference between a_t and the sum of a_l and a_c is representative of the uncertainty in the spatial velocity derivatives introduced by the 3D-PTV post-processing. As described in Luethi et al. (2005), a_t is calculated based on the information along particle trajectories and is therefore independent of the interparticle distance. The resolution of the acceleration can be estimated from the camera pixel size and frame rate to be less than 3m/s^2 for both a_t and a_l. To quantify the uncertainty in the spatial velocity derivatives, σ is defined as:

$$\sigma = \frac{\sqrt{\sum_{i=1}^{N} \left(a_{t,i} - (a_{l,i} + a_{c,i})\right)^2}}{N}, \quad (3)$$

where N is the length of the particle track in time steps. For each time step, the relative uncertainty in the velocity derivatives is estimated by taking the mean dimensionless variance $\sigma/|\bar{a}_t|$ from that time step, as shown in Fig. 4 (b) for the x, y and z components of the slow-pitching motion of the low-aspect-ratio plate. The relative uncertainties in the spatial velocity derivatives for the experiment are therefore estimated as 0.13, 0.14 and 0.18 for the x, y and z components of acceleration, respectively. Note that these relative uncertainties are of the same order as the total and temporal derivatives in the system.

3 Results

A number of questions regarding vortex growth rates and interaction were proposed in the introduction and have been addressed by comparison of direct force and 3D-PTV measurements for the various test cases. Although many runs of each test case were taken and the repeatability of the test cases was ascertained, the results presented in the subsequent subsections are from single runs in which the results of the direct force and 3D-PTV measurements correspond to each other. In the first subsection, a comparison between the time-resolved lift coefficients for the nominally two-dimensional and low-aspect-ratio plates is performed. Here, the z-convection term of Eq. 2 is considered while the effect of the tip vortex on the leading-edge-vortex development is investigated via spanwise circulation distributions over the pitching period. In the second subsection, the timescales for leading-edge-vortex and tip-vortex growth are examined by integrating the spanwise circulation distribution over the span as well as by comparing the iso-surfaces of constant vorticity for the slow- and fast-pitching motions. Finally, in the third subsection, Lagrangian particle tracks highlight the interaction between the leading-edge and tip vortices. Here, the contribution of the z-stretching term of Eq. 2 to the overall vortex topology is considered.

3.1 The effect of the tip vortex on leading-edge-vortex growth

Using the force balance, the instantaneous lift coefficient (C_L), non-dimensionalized by freestream velocity U_∞ and planform area, was measured for the slow- and fast-pitching motions of both the nominally two-dimensional and low-aspect-ratio plates. C_L of the slow- and fast-pitching motions of the nominally two-dimensional and low-aspect-ratio plates are plotted alongside the instantaneous pitch angle in Fig. 5. As the pitching motions are sinusoidal, the angular acceleration history is identical to the angular position history. Therefore, the maximum accelerations which lend to non-circulatory-like forces occur at the extremes of 0° and 45°. In Fig. 5a, the lift coefficient increases linearly early on for both plates, reaching a

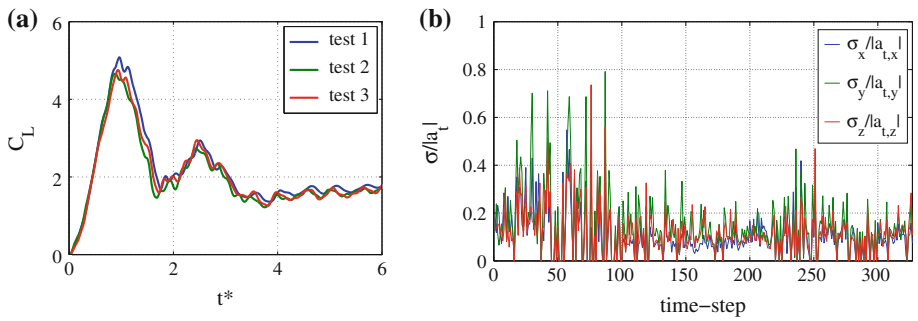

Fig. 4 **a** Lift coefficient from three runs of the fast-pitching motion of the nominally two-dimensional plate. The force signals were processed using a technique similar to that employed by Jones and Babinsky (2011). **b** Mean $\sigma/|\bar{a}_t|$ for the x, y, and z components of acceleration at each time step for the slow-pitching motion of the AR=4 plate (*right*), with time step 0 corresponding to the beginning of the pitching motion

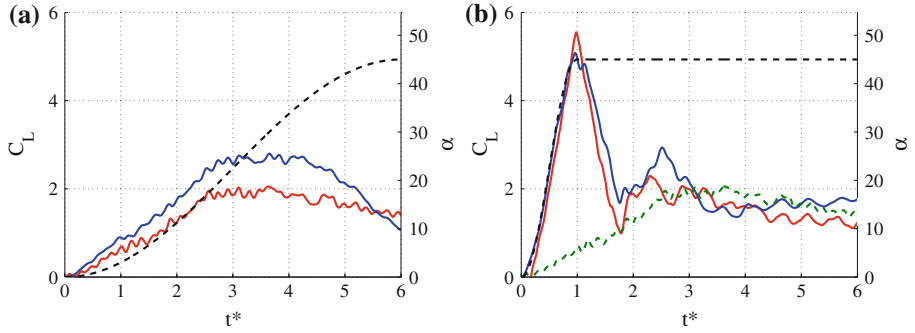

Fig. 5 The lift coefficient as measured by the force balance for the slow- (**a**) and fast-pitching (**b**) motion of the low-aspect-ratio (*red*) and nominally two-dimensional (*blue*) plates, plotted alongside the instantaneous pitch angle of the plates (*black dashed line*). The α-ordinate is scaled such that $C_L = 2\pi\alpha$; note the good agreement early on in the accelerations implying strong two-dimensionality for low-aspect-ratio cases. C_L for the slow-pitching motion of the low-aspect-ratio plate is plotted with a *dashed green line* in (**b**) to highlight the similarity between the force curves of the slow- and fast-pitching motions of the low-aspect-ratio plates for $t^* > 3$. The force signal was processed using a technique similar to that employed by Jones and Babinsky (2011)

maximum at around $t^* = 3$, where $t^* = tU_\infty/c$. After the broad lift peak, the lift was found to decrease gradually towards a steady-state value. In contrast, the fast-pitching motion demonstrates a sharp increase in lift with a peak at $t^* = 1$; see Fig. 5b. Due to the high effective reduced frequency of the fast-pitching motion, it is hypothesized that the lift peak at $t^* = 1$ is primarily due to non-circulatory-like (added-mass) effects. The lift peak in the fast-pitching motion is then followed by a rapid decrease in lift, and by $t^* = 3$, the force settles out to values similar to those seen at $t^* = 3$ in Fig. 5a for the slow-pitching motion. In fact, the lift variations on the low-aspect-ratio plate for both the slow- and fast-pitching motions are remarkably similar from $t^* = 3$ through $t^* = 6$, especially when considering the dramatic difference in the pitch variation for these two cases. Comparing C_L to the lift coefficient predicted by the two-dimensional quasi-steady formulation ($C_L = 2\pi\ \alpha$), good agreement is found in the range between $0 < t^* < 3$ for the slow-pitching motion and between $0 < t^* < 1$ for the fast-pitching motion. This result implies strong two-dimensionality early on in the acceleration of the finite-aspect-ratio plates.

Since the slow-pitching motion of the nominally two-dimensional and low-aspect-ratio plates had significantly lower pitch accelerations, the lack of a strong non-circulatory spike in lift was of no surprise. It was therefore hypothesized that the broad lift peak beginning at $t^* = 3$ was due primarily to circulatory effects. To test this hypothesis, it was assumed, based on the results from Pitt-Ford and Babinsky (2012), that the circulatory lift was as a first approximation caused only by the leading-edge vortex. To obtain a first-order estimate of the circulatory lift due to the leading-edge vortex, the instantaneous circulation of the leading-edge vortex Γ_{LEV} was calculated from a numerical integration of counterclockwise $z-$ vorticity ($\omega_{z,\ ccw}$) such that:

$$\Gamma_{LEV} = \iint_A \omega_{z,ccw} dA. \tag{4}$$

Note that as the leading-edge vortex is connected to the shear layer during the leading-edge-vortex formation process, the circulation of the shear layer is included in the calculation of Γ_{LEV}. The integration in Eq. 4 was evaluated numerically on 11 evenly spaced planes normal to the plate surface within the measurement volumes shown in Fig. 3. The 11 planes were spaced $z/c = 0.1$ apart, with the bottom-most plane coincident with the tip of the low-aspect-ratio plate and the top-most plane at a non-dimensional spanwise position $z/c = 1$. Refer to 2 (b) for the location of the origin of the z-axis with respect to the low-aspect-ratio plate. This spanwise region of $0 \leq z/c \leq 1$ is defined as the tip region, as described in the work by Jardin et al. (2012). To generate a first-order approximation of the local lift due to the instantaneous circulation of the leading-edge vortex, the spanwise circulatory lift coefficient of the leading-edge vortex was defined as:

$$C_{l_{LEV}} = \frac{2\Gamma_{LEV}}{U_\infty c}. \tag{5}$$

Figure 6 shows the spanwise distribution of the circulatory lift due to the instantaneous circulation of the leading-edge vortex. As expected, the spanwise lift is evenly distributed for the nominally two-dimensional plate. For the low-aspect-ratio plate, the spanwise lift decreases towards the tip. This result is similar to the results seen by Ringuette et al. (2007) and suggests that there is a strong interaction between the tip-vortex and leading-edge-vortex development in this near-tip region. As stated earlier, the z-convection term from Eq. 2 provides a mechanism to redistribute the leading-edge vorticity in the spanwise direction. To measure the contribution of the z-convection term on the reduction of $C_{l_{LEV}}$ in the vicinity of the tip,

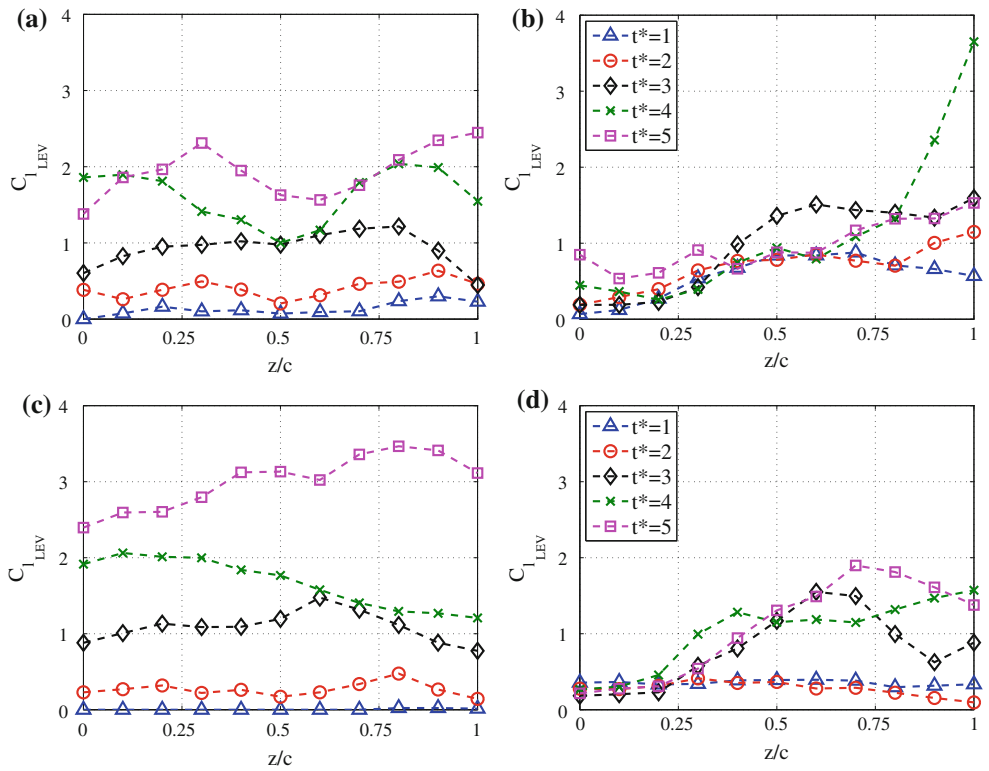

Fig. 6 The spanwise lift coefficient due to the instantaneous circulation of the leading-edge vortex plotted against non-dimensional span for the slow- (*top*) and fast-pitching (*bottom*) motions of the nominally two-dimensional (*left*) and low-aspect-ratio (*right*) plates. This spanwise lift coefficient is plotted at dimensionless times $t^* = 1 - 5$. $z/c = 0$ corresponds to the tip of the low-aspect-ratio plate

regions of instantaneous spanwise velocity are identified through iso-surfaces of non-dimensional velocity ($w^* = w/U_\infty$) shown in Fig. 7. Here, one can observe that for both the slow- and fast-pitching motions, the spanwise velocity always moves from tip to mid-span in the tip region, and primarily as a function of pitch angle. Therefore, the z-vorticity feeding the leading-edge vortex in the tip region will be convected inboard from the tip towards the mid-span, lowering the circulation of the leading-edge vortex in the tip region as observed in Fig. 6. Furthermore, in Fig. 7a, d, note that the inboard-directed spanwise velocity is observed at $t^* = 0.3$ for the fast-pitching motion while inboard-directed velocity is not observed until approximately $t^* = 1.7$ for the slow-pitching motion. This observation suggests that for the low-aspect-ratio plate, the inboard-directed flow evolution is correlated with the pitch angle. This pitch-angle correlation, however, is further investigated in the following section.

3.2 Timescales of vortex growth

The spanwise distribution of the LEV lift, as shown in Fig. 6, was numerically integrated at each time step over the span to yield the total circulatory lift coefficient due to the LEV. For the nominally two-dimensional plate, this integration was essentially an average of the spanwise lift distribution. For the low-aspect-ratio plate, symmetry about the mid-span was assumed and the lift distribution in the $1 \leq z/c \leq 3$ region was assumed to be constant and equal to the spanwise lift coefficient at $z/c = 1$. In Fig. 8 (a), there is a general agreement between the magnitude of the lift peaks of the leading-edge-vortex lift and the broad lift peaks of the direct force measurements for both the nominally two-dimensional and low-aspect-ratio plates. This order-of-magnitude agreement supports our hypothesis that the forces in the slow-pitching motion are largely due to the circulatory effects of the leading-edge vortex. Of interest is the sharp drop in the circulatory lift of the low-aspect-ratio plate shortly after $t^* = 4$, which qualitatively agrees with the timing of the leading-edge-vortex eruption observed by Yilmaz and Rockwell (2012) on a rectangular plate of aspect ratio two. In addition, note that the decay in C_L of the nominally two-dimensional plate at $t^* > 4$ is correlated with a drop in $C_{L,LEV}$. In Fig. 8b, there is no agreement between the leading-edge-vortex lift and the measured lift peak at $t^* = 1$. Thus, the lift peak observed at $t^* = 1$ in the fast-pitching motion is not caused by the instantaneous circulation of the LEV. As this lift peak is in phase with the acceleration of the fast-pitching motion, it is

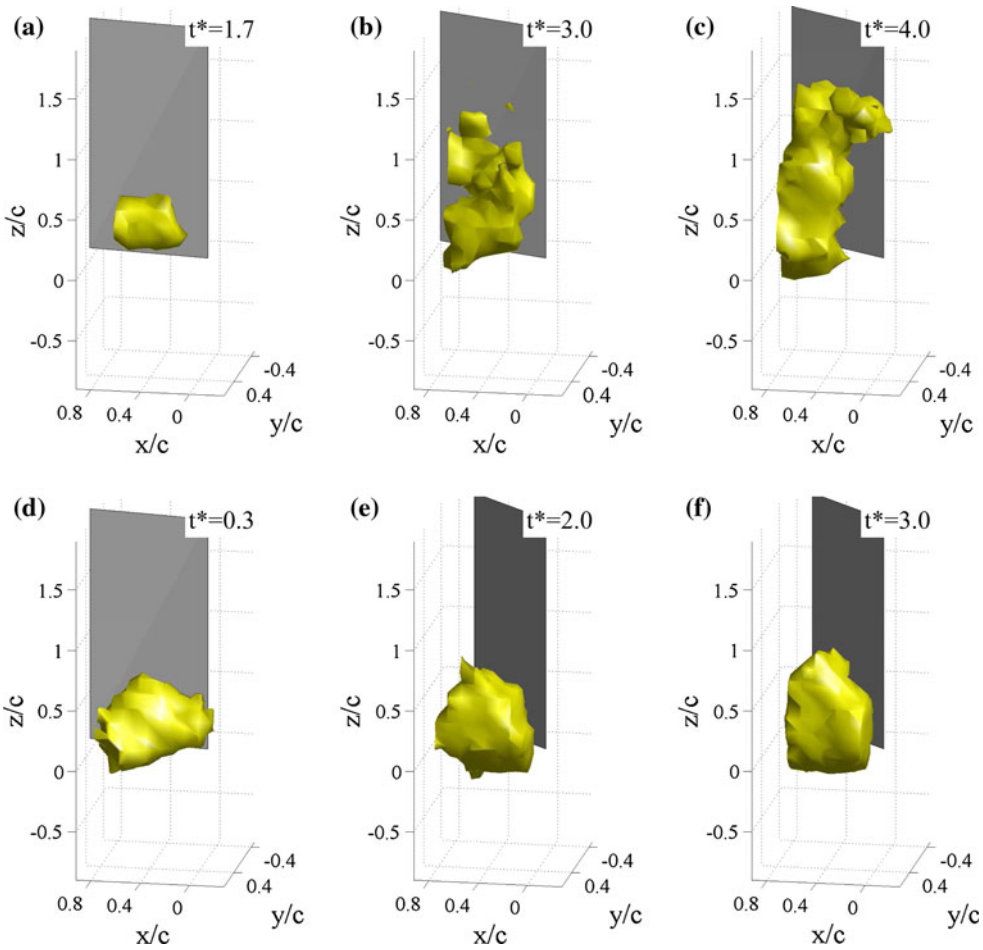

Fig. 7 Iso-surfaces of inboard-directed non-dimensional spanwise velocity ($w^* = 0.375$) for the slow- (**a**–**c**) and fast-pitching (**d**–**f**) motions of the low-aspect-ratio plate. Note that there is no significant outboard velocity at the dimensionless times shown. Oncoming flow is in the positive x-direction. Note the similarities in the inboard-directed flow despite the varying dimensionless times, implying a strong pitch-angle correlation

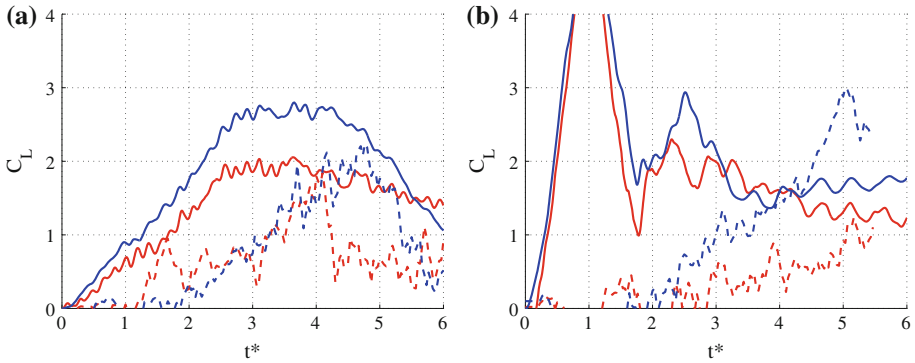

Fig. 8 Lift coefficient as measured by the force balance (*solid*) and lift coefficient based on leading-edge-vortex circulation (*dashed*) plotted against t^* for the slow- (**a**) and fast-pitching (**b**) motions of the nominally two-dimensional (*blue*) and low-aspect-ratio (*red*) plates

likely that the lift peak is due to non-circulatory-like effects. Furthermore, when comparing the leading-edge-vortex lift for the slow- and fast-pitching motions of the nominally two-dimensional plate in Fig. 8, one can observe that the magnitude and growth rate of $C_{L_{LEV}}$ are similar despite the dramatically different kinematics. This suggests that for a two-dimensional pitching plate, the leading-edge-vortex growth is correlated to convective time (t^*) and such growth is relatively independent of pitch angle. This convective-time correlation is in agreement with results from Baik et al. (2012), where, for example, the leading-edge vortex observed at a reduced frequency of $k = 0.314$ ($t/T = 0.25$) is similar to the leading-edge vortex observed for $k = 0.628$ ($t/T = 0.50$).

Returning to Fig. 8, a pitch-angle independence is not observed for the leading-edge-vortex growth on the low-aspect-ratio plates, where the growth of leading-edge-vortex lift in the tip region is retarded far more for the fast-pitching motion. This is in agreement with recent results from Visbal (2012), who found that there was a phase delay in the flow-field evolution at high pitch rates for an aspect-ratio-two rectangular plate. To further investigate the

difference in leading-edge-vortex growth in the tip region of the low-aspect-ratio plate, a methodology similar to that employed by Kim and Gharib (2010) is used and iso-surfaces of vorticity are plotted at a constant magnitude in order to qualitatively identify changes in vortex size and position. Iso-surfaces of non-dimensional z-vorticity ($\omega_z^* = \omega_z c/U_\infty$) and non-dimensional xy-vorticity (ω_{xy}^*) are plotted in Fig. 9 for the slow- and fast-pitching motions of the low-aspect-ratio plate. The non-dimensional xy-vorticity is defined as:

$$\omega_{xy}^* = \frac{\left(\sqrt{\omega_x^2 + \omega_y^2}\right)c}{U_\infty}. \quad (6)$$

Recall from Fig. 7 that inboard-directed spanwise velocity was observed at $t^* = 0.3$ for the fast-pitching motion and at $t^* = 1.7$ for the slow-pitching motion. In Fig. 9a, d, iso-surfaces of z—and xy—vorticity reveal that a tip vortex is observed as early as $t^* = 0.3$ for the fast-pitching motion while substantially later ($t^* = 1.7$) for the slow-pitching motion. The early tip vortex observed in the fast-pitching motion implies that the tip-vortex growth is correlated to the pitch angle. The connection between the evolution of spanwise velocity seen in Fig. 7 and the development of the tip vortex seen in Fig. 9 indicates that the tip vortex is correlated with the inboard-directed velocity observed in the tip region, and thus the inboard convection of leading-edge vorticity as well.

The impact of the inboard convection of leading-edge vorticity on the leading-edge-vortex growth in the tip region is evident throughout the measurements. For the slow-pitching motion, the leading-edge vortex has an arched shape at $t^* = 3.0$, as seen in Fig. 9b. At $t^* = 4.0$ in Fig. 9c, the arch of the leading-edge vortex is even more pronounced, and the vortex topology qualitatively matches the flow structures visualized by Yilmaz and Rockwell (2012) at a similar non-dimensional time. For the fast-pitching motion, the effect of the tip vortex on the leading-edge-vortex growth is most pronounced at $t^* = 2.0$, as seen in Fig. 9e, where significant levels of leading-edge vorticity exist only well inboard of the tip. Figure 9f then shows that at $t^* = 3.0$, the leading-edge vortex has an arched shape qualitatively similar to that of the slow-pitching motion at $t^* = 4.0$. Additionally, there is a structure of xy-vorticity well inboard of the tip at $t^* = 3.0$ of the fast-pitching motion and $t^* = 4.0$ of the slow-pitching motion. This structure is qualitatively similar to

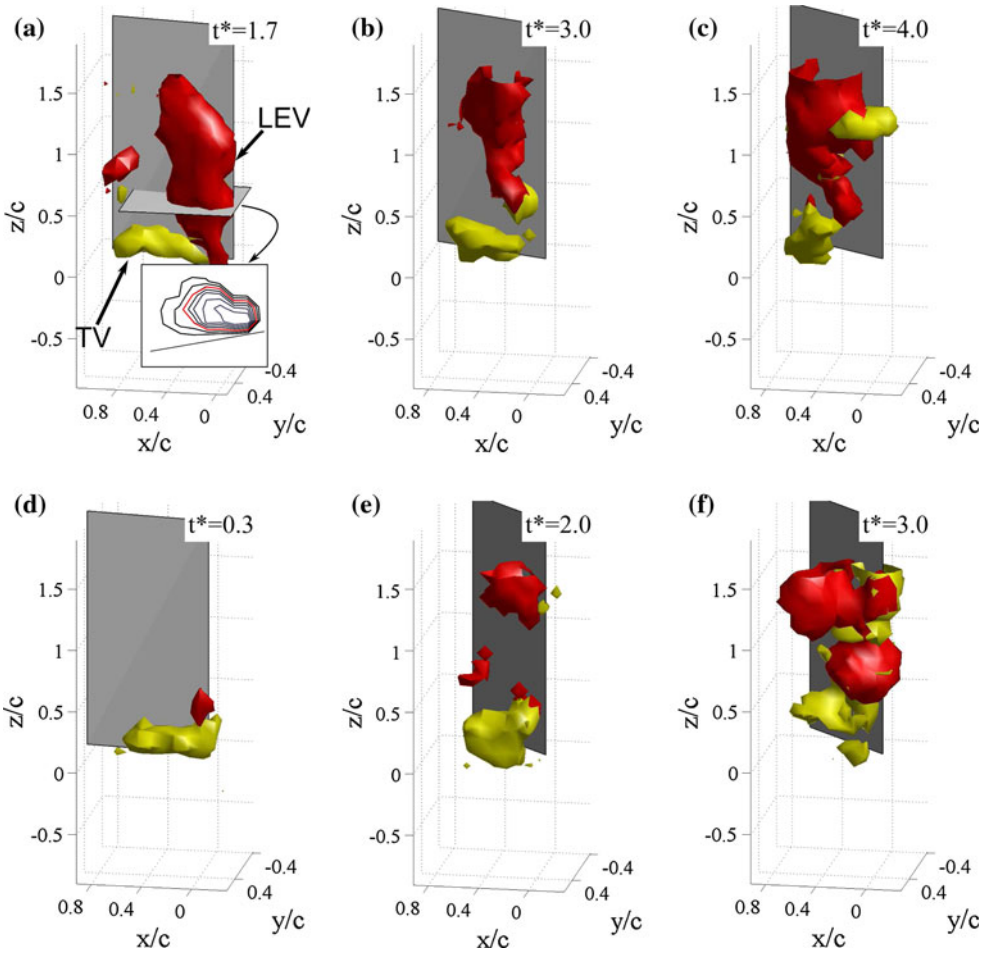

Fig. 9 Qualitative comparison of non-dimensional z-vorticity (*red*) and non-dimensional xy-vorticity (*yellow*) for the slow- (**a**–**c**) and fast-pitching (**d**–**f**) motions of the low-aspect-ratio plate. Iso-surfaces are plotted at constant $\omega_z^* = \omega_{xy}^* = 2.5$. Oncoming flow is in the positive x-direction. The leading-edge vortex (LEV) and tip vortex (TV), as well as a vorticity contour with $\omega_z^* = 2.5$ highlighted in *red*, are indicated in (**a**). Note that specific time steps have been selected to demonstrate how the tip-vortex growth is correlated with pitch angle, that the leading-edge-vortex growth on a low-aspect-ratio plate is less correlated with pitch angle, and finally the effect of leading-edge-vortex compression at the mid-span position

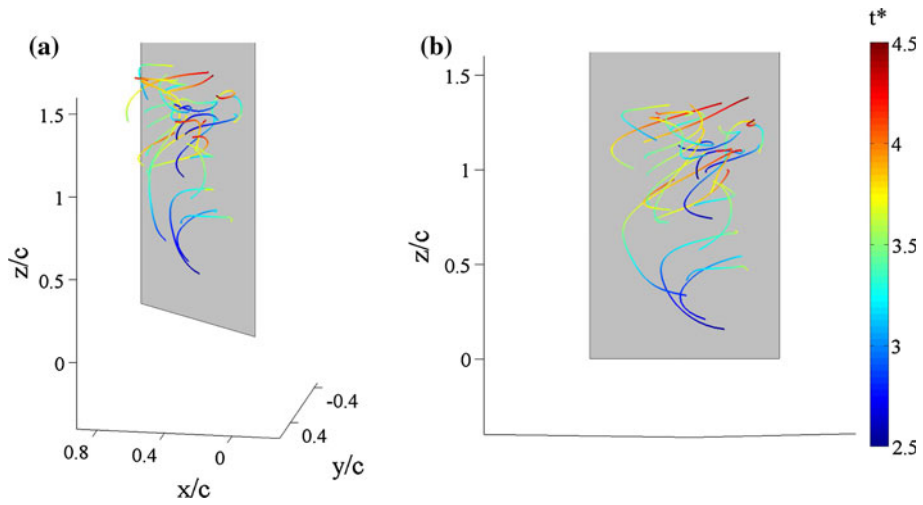

Fig. 10 **a** Isometric and **b** plate-normal views of filtered Lagrangian particle tracks of the slow-pitching motion of the low-aspect-ratio plate from $t^* = 2.5$–4.5. Tracks are coloured by convective time to qualitatively show both direction of motion and velocity. The angle of attack of the plate shown is 38.4° which corresponds to the plate position at $t^* = 4.5$. Oncoming flow is in the positive x-direction

the large streamwise oriented structure observed by Yilmaz and Rockwell (2010) on an aspect-ratio-two rectangular flat plate and is correlated with the development of the arched leading-edge vortex observed at these times. By contrasting the differences in the leading-edge-vortex growth in the tip region of the low-aspect-ratio plate for the slow- and fast-pitching motions, it is evident that the leading-edge-vortex growth on a low-aspect-ratio plate is not strictly correlated with the convective timescale as is the case for a nominally two-dimensional plate and is influenced by the instantaneous pitch angle as well.

3.3 Tip vortex causes leading-edge-vortex compression

To provide further insight into the leading-edge and tip-vortex interaction, Lagrangian particle tracks coloured by dimensionless convective time are plotted in Fig. 10. Analysis of the Lagrangian flow field allows for the tracking of the transport of fluid elements that are contained in the leading-edge vortex. Particles which were tracked for less than 20 time steps were removed to make the visualization less crowded. A velocity filter removing tracks with an average x-velocity greater than 0.1 m/s was also employed for visualization purposes. Only tracks which are located in the near-wake of the plate remain after this filtering procedure. From Fig. 10, it is observed that, in the slow-pitching motion of the low-aspect-ratio plate, there is an inboard-directed flow of particles caught in the leading-edge vortex from $t^* = 2.5$–4.5. In fact, in this period of time, no particles are found to convect from the leading-edge vortex into the tip vortex. Recall from Fig. 8 that $t^* = 2.5$–4.5 is roughly the period of time in which the bulk of the leading-edge vorticity grows. Thus, it can be concluded that as the leading-edge vortex grows it remains distinct from the tip vortex.

Recall from the vorticity transport formulation that if negative, the z-stretching term $\omega_z \, \partial w/\partial z$ from Eq. 2 implies a compression of the leading-edge vortex. The particle tracks in Fig. 10 reveal a decrease in the inboard-directed velocity as particles approach the centre span. The decrease in inboard-directed velocity shows that the gradient $\partial w/\partial z$ is negative, suggesting that the leading-edge vortex is undergoing compression. Thus, although the leading-edge and tip vortices grow distinct from one another, the inboard convection of leading-edge vorticity—which is correlated with the presence of the tip vortex—is responsible for leading-edge-vortex compression at the mid-span position. This compression results in the arched shape of the leading-edge vortex visualized in Fig. 9b, c for the slow-pitching motion and Fig. 9f for the fast-pitching motion.

4 Conclusions

A nominally two-dimensional flat plate, as well as a flat plate of aspect ratio four, was pitched at a Reynolds number based on chord of 10,000. Two half-cosine pitching profiles were investigated. The fast-pitching profile with reduced frequency $k = 1.57$ completed the pitch motion from 0° to 45° in non-dimensional time $t^* = 1$, while the slow-pitching profile with $k = 0.26$ pitched from 0° to 45° in $t^* = 6$. The instantaneous lift on the plates was acquired using a six-component force and moment sensor. Simultaneously, the instantaneous flow-field on the suction side of the plates was quantified using 3D-PTV. The vorticity transport equation was introduced, and the implications of leading-edge-vortex convection, tilting and stretching were addressed.

Four conclusions have been drawn from the experimental campaign. The first conclusion is that two-dimensional leading-edge-vortex growth, as seen for the nominally two-dimensional plate, is correlated with a convective timescale non-dimensionalized by freestream velocity and chord. Thus, two-dimensional leading-edge-

vortex growth is independent of pitch angle. This convective timescale correlation is supported through the similarity between the LEV lift evolution of the slow- and fast-pitching motions of the nominally two-dimensional plate.

The second conclusion is that the inboard-directed spanwise velocity in the tip region is correlated with the tip vortex, where the tip region is defined as the spanwise region between the tip and one chord length inboard of the tip. Spanwise velocity is observed to remain directed inboard throughout the measurements for both the slow- and fast-pitching motions. Thus, throughout the motions, vorticity generated at the leading edge is convected inboard. As a result, the leading-edge-vortex circulation is reduced in the tip region.

The third conclusion is that tip-vortex growth is strongly correlated with pitch angle. For the fast-pitching motion, a coherent tip vortex is observed at $t^* = 0.3$, while for the slow-pitching motion, a coherent tip vortex is not observed until $t^* = 1.7$. Thus, the leading-edge-vortex growth is retarded in the vicinity of the tip for the high reduced frequency of $k = 1.57$ where the tip vortex is found to outpace the LEV. Therefore, it can be concluded that the leading-edge-vortex growth on a low-aspect-ratio plate is not strictly correlated with a convective timescale as is the case for a nominally two-dimensional plate.

The fourth and final conclusion is that the leading-edge and tip vortices grow distinct from one another. Lagrangian particle tracks reveal that at no time in the leading-edge-vortex development do particles convect from the leading-edge vortex into the tip vortex. However, similar to the pitching case of an aspect-ratio-two flat plate investigated by Yilmaz and Rockwell (2012), as the leading-edge vortex grows, it experiences negative vortex stretching (vortex compression) caused by the inboard flow which is correlated with the presence of the tip vortex. Thus, although the tip- and leading-edge vortices remain distinct of one another, the tip vortex is found to influence the leading-edge-vortex dynamics, particularly at higher reduced frequencies.

Acknowledgments The authors acknowledge the funding provided by the Natural Science and Engineering Research Council of Canada. The authors would also like to thank the constructive feedback from all three reviewers.

References

Baik Y, Bernal L, Granlund K, Ol M (2012) Unsteady force generation and vortex dynamics of pitching and plunging aerofoils. J Fluid Mech. doi:10.1017/jfm2012.318

Barnes C, Visbal M (2012) High-Fidelity Simulations of a Hovering Wing. In: 42nd AIAA fluid dynamics conference and exhibit, New Orleans, Louisiana, USA. AIAA 2012-2699

Beem H, Rival D, Triantafyllou M (2012) On the stabilization of leading-edge vorticies with spanwise flow. Exp Fluids 51:511–517

Birch D, Lee T (2005) Investigation of the near-field tip vortex behind an oscillating wing. J Fluid Mech 544:201–241

Carr Z, Chen C, Ringuette M (2012) The effect of aspect ratio on the three-dimensional vortex formation of rotating flat-plate wings. In: 50th AIAA Aerospace Sciences Meeting; Nashville, Tennessee, USA. AIAA 2012-0912

Feng Y, Goree J, Liu B (2011) Errors in particle tracking velocimetry with high-speed cameras. Rev Sci Instrum 82:053707

Garmann D, Visbal M, Orkwis P (2012) Three-dimensional flow structure and aerodynamic loading on a low aspect ratio, revolving wing. In: 42nd AIAA Fluid Dynamics Conference and Exhibit; New Orleans, Louisiana, USA. AIAA 2012-3277

Jardin T, Farcy A, David L (2012) Three-dimensional effects in hovering flapping flight. J Fluid Mech 702:102–125

Jones AR, Babinsky H (2011) Reynolds number effects on leading edge vortex development on a waving wing. Exp Fluids 51:197–210

Kähler CJ, Scharnowski S, Cierpka C (2012) On the uncertainty of digital piv and ptv near walls. Exp Fluids 52:1641–1656

Kim D, Gharib M (2010) Experimental study of three-dimensional vortex structures in translating and rotating plates. Exp Fluids 49:329–339

Kim D, Gharib M (2011) Flexibility effects on vortex formation of translating plates. J Fluid Mech 677:255–271

Kinzel M, Wolf M, Holzner M, Lüthi B, Tropea C, Kinzelbach W (2011) Simultaneous two-scale 3D-PTV measurements in turbulence under the influence of system rotation. Exp Fluids 51:75–82

Lentink D, Dickinson MH (2009) Rotational accelerations stabilize leading edge vortices on revolving fly wings. J Exp Biol 212:2705–2719

Luethi B, Tsinober A, Kinzelbach W (2005) Lagrangian measurement of vorticity dynamics in turbulent flow. J Fluid Mech 528: 87–118

Ozen C, Rockwell D (2012) Three-dimensional vortex structure on a rotating wing. J Fluid Mech

Pitt-Ford C, Babinsky H (2012) Lift and the leading edge vortex. In: 50th AIAA Aerospace Sciences Meeting; Nashville, Tennessee, USA. AIAA 2012-0911

Ringuette MJ, Milano M, Gharib M (2007) Role of the tip vortex in the force generation of low-aspect-ratio normal flat plates. J Fluid Mech 581:453–468

Visbal M (2011) Three-dimensional flow structure on a heaving low-aspect-ratio wing. In: 49th AIAA Aerospace Sciences Meeting. Orlando, Florida, USA. AIAA 2011-219

Visbal M (2012) Flow structure and unsteady loading over a pitching and perching low-aspect-ratio wing. In: 42nd AIAA Fluid dynamics conference and exhibit. New Orleans, Louisiana, USA. AIAA 2012-3279

Yilmaz T, Ol M, Rockwell D (2010) Scaling of flow separation on a pitching low aspect ratio plate. J Fluids Struct 26:1034–1041

Yilmaz TO, Rockwell D (2010) Three-dimensional flow structure on a maneuvering wing. Exp Fluids 48:539–544

Yilmaz TO, Rockwell D (2012) Flow structure on finite-span wings due to pitch-up motion. J Fluid Mech 691:518–545